

Influence of electrode arrangements on Electrohydrodynamics and transport phenomenon within water and porous samples connected to rectangular duct

Suwimon Saneewong Na Ayuttaya^a, Phadungsak Rattanadecho^{b,*}

^a Department of Mechanical Engineering, Academic Division, Chulachomklao Royal Military Academy, Nakhon-Nayok, 26001, Thailand

^b Center of Excellence in Electromagnetic Energy Utilization in Engineering (CEEE), Department of Mechanical Engineering, Faculty of Engineering, Thammasat University, Khlong Luang, Pathum Thani, 12120, Thailand

ARTICLE INFO

Keywords:

Electrode arrangement
Heat transfer enhancement
Swirling flow
Shear flow
Porous sample

ABSTRACT

A numerical study based on the concept of conjugate transport phenomena analysis has been developed for the investigation of heat transfer and fluid flow within a rectangular duct and a sample by Electrohydrodynamics technique. High electrical voltage and average velocity of inlet hot-airflow are applied at 20 kV and 0.1 m/s, respectively. Electrode arrangements or angle between electrode and ground are varied in a range of $\theta = 0\text{--}360^\circ$. The effect of swirling flow on EHD-enhanced heat transfer is also examined. The results show that electric field from various angles can induce the difference swirling flow pattern. By fluid flow within the sample is depended on the swirling flow and hot-airflow direction. Besides the shear flow effect, swirling flow is affected by temperature distribution. Therefore, it affects the sample. Furthermore, fluid flow from swirling flow effect and sample properties is the main mechanism of natural convection and conduction modes, respectively. Finally, the comparison of heat transfer enhancement between water sample and porous sample are also presented.

1. Introduction

Conventional drying technique is usually involved high temperatures; this technique is widely used in food products. However, physical and chemical properties are changed due to produce undesirable. Furthermore, its drying period is long resulting in large energy consumption. The most important thing in industries except for producing the high-quality products, there is to increase productivity and reduce production cost. In fact, drying technique is involved with conventional heat transfer by air, it is the most common medium used to transfer energy in thermal food products. It is usually blown at the surface of the food to ensure by heat treatment since drying, chilling, boiling and freezing are the processes mainly concerned by these convective heat transfers [1–3]. The recent development trends in heat transfer technique are focusing on conventional or hot-air drying cooperating with other techniques such as microwave, vacuum, infrared and Electrohydrodynamics (EHD) [4–8]. In general, several techniques of industrial products are related to heat transfer technique either by using energy from other sources resulting in low production costs. The microwave heating technique takes place inside the material, the penetrated depth of which governs how strongly the microwave energy absorbed. However, it is known that the heat dissipated from the

microwave technique depended on many parameters it is known that result in poor quality products when it is not properly applied [9]. In the vacuum, a technique can reduce operating times and higher end-product quality but fundamental of vacuum technique is the operating pressure to control of the product below a prescribed limit [10]. From infrared radiation, it is transmitted through water at a short wavelength while it is absorbed on the surface at a long wavelength [11]. One way to improve thermal efficiency is to extend heat transfer area and increase the flow velocity. The heat transfer enhancement technique utilizing electrostatic force generated from the polarization of dielectric fluid or EHD can be one of the most promising methods among various active techniques because of its several advantages. This technique deals with the interdisciplinary field with subjects concerning the interactions between electric and flow fields. When an electrical voltage is exposed to airflow, ions from a sharp electrode move forwards to the ground. An ionic wind or primary flow is formed when air ions are accelerated by an electric field and exchange momentum with neutral air molecules. It is because ionic winds can generate flow with no moving parts and have low power consumption. As a result, the momentum of airflow is enhanced [12]. Meanwhile, shear flow effect which is occurred by velocity difference between uncharged and charged air induces the uncharged air to become secondary flow or

* Corresponding author.

E-mail address: ratphadu@engr.tu.ac.th (P. Rattanadecho).

swirling flow.

In order to improve convective heat transfer, some researchers are studying seriously in EHD technique with flow control [13–19]. Dukravich et al. [13] studied a mathematical model and an explicit finite-difference for two-dimensional laminar steady flow and solidification of an incompressible, viscous and electrically conducting. The system of governing EHD equations was derived from a combination of Maxwell's equations and the Navier-Stokes equations including thermally induced buoyancy, latent heat release, and Joule heating. The numerical results demonstrated the existence of strong electrothermoconvective motion in the melt and quantify its influence on the amount of accrued solid, deposition pattern of the electrically charged particles inside the accrued solid and the melt/solid interface shape. Go et al. [17] analytically and experimentally studied of heat transfer from a flat plate. Corona discharges were generated between a steel wire and copper-tape electrode pair on a flat plate, perpendicular to the bulk flow direction such that the ensuing ionic wind was in the direction of the bulk flow. The magnitude of the corona current and the heat flux on the flat plate were varied. The result found that the heat transfer coefficient was shown to be related to the fourth root of the corona current and heat transfer enhancement was seen to be solely a hydrodynamic effect. Variation of the spacing between electrodes demonstrates that while the local peak enhancement was largely unaffected, the area of heat transfer enhancement was dependent on this spacing. Kasayapanand [18] numerical studied the electric field effect on natural convection in the square enclosures with the single fin and multiple fins. The interactions electric, flow and temperature fields were analyzed using a computational fluid dynamics technique. The parameters considered the supplied voltage, Rayleigh number, size of the enclosure, electrode arrangements, number of fins and fin length. The result shown that the flow and heat transfer enhancements were the decreasing function of Rayleigh number, the heat transfer coefficient was substantially improved by the electric field effect especially at the high number of fins and longfin length. In addition, the maximum average velocity and heat transfer enhancement occurred at the different electrode arrangements for the single fin and multiple fins.

For several years our research group tried to increase the convective heat transfer subject to EHD technique [20–22] such as Chakranond and Rattanadecho [20] experimentally investigated the influences of electrical voltage on the heat and mass transfer in porous packed bed subjected to EHD drying. The results showed that the heat and mass transfer rate in the packed bed was increased when using EHD. Furthermore, the convective heat transfer coefficient and drying rate were considerably enhanced with the strength of electric field influencing swirling flow. Saneewong Na Ayuttaya et al. [21] studied electric field distribution, characteristics of swirling flow and effect of inlet velocity. The numerical results showed that the difference of electrode and ground arrangements influenced the swirling flow behavior dominantly due to the characteristics of Coulomb force or electric body force which was affected by the electric field. The strength of swirling flow was decreased when inlet velocity was increased because inertial force was superior to the electric body force. Moreover, the idea behind this work can be used as guidance for the special design of EHD application processes in the future. It can be seen that our group studies flow phenomena under electric field in order to increase the swirling flow. The benefit of swirling flow is directly related to heat transfer

enhancement within a sample. Various types of sample occur in many industries such as food, ceramic and wood. The most of sample is the porous material or porous medium. The porous medium is a material that consists of a solid matrix with an interconnected void. Based on the complexity of interface problem, the heat transfer and swirling flowing past it is a conjugate transport phenomenon. The heat transfer between a body and a fluid flowing past it is a conjugate problem, because the heat transfer inside the body is governed by the elliptical Laplace equation or by the parabolic differential equation, while the heat transfer inside the fluid is governed by the elliptical Navier-Stokes equation or by the parabolic boundary layer equation. The solution of such problem gives the temperature and heat flux distributions on the interface, and there is no need for a heat transfer coefficient.

From the literature review of conjugate approach [23–27], it is essential to simulate all of this electric field, flow field and temperature field systematically but there are few studied on EHD technique with the conjugate approach. In this study, a rectangular duct flow model is used to simulate the swirling flow and heat transfer enhancement in the specified domain. Moreover, electrode arrangements are varied the angle between electrode and ground, in order to study the suitable arrangements for enhancing the fluid flow and temperature distribution within sample. The natural convection or fluid flow within sample has been studied. Finally, comparison of heat transfer and fluid flow within water sample and water porous sample are presented.

2. Modeling analysis

This rectangular channel comprised of main three parts, the first, second and third parts are the electric field, fluid flow, and heat transfer models, respectively. The dimension of rectangular channels is 2.8 m (long) \times 0.3 m (high). In order to study effect within the sample, it is placed at the lower of rectangular duct and the top surface is exposed to the hot-airflow. By sample is connected to the rectangular duct. The dimension of the sample is 10 cm \times 5 cm, as shown on Fig. 1. Furthermore, the interface between hot-airflow and sample is investigated by the concept of conjugate approach. Within the rectangular duct, electrode and ground are 0.5 mm (diameter). The position of the ground is always fixed at $x = 0$ m and $y = 0$ m. The displacement between electrode and ground is $d = 4$ cm. The angle between electrode and ground (θ) is varied in clockwise direction from 0 to 360°. A sub-domain is used for the entire simulation space which made up the inside a rectangular duct. By using the electrical, charge transport, temperature and fluid equations are solved, the classical properties of hot-airflow, water and solid are shown in Table 1 [21 and 28] and the thermal properties of hot-airflow, water and solid are shown in Table 2 [21 and 28]. In this study, the porous sample is a saturated porous packed bed; it consisted of single size glass beads with only water in voids.

3. Model approach

A numerical modeling based on conjugate approach has been formulated to predict the fluid flow and temperature distribution within the rectangular duct and predict the transport phenomenon with the sample. Three boundary conditions of the electric field, fluid flow, and heat transfer models are shown in Fig. 2.

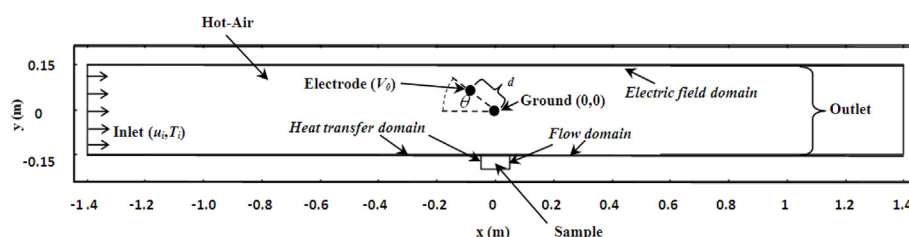


Fig. 1. Model geometry for analysis.

Table 1
Classical properties.

Modeling parameter	b (m ² /V.s)	ε (F/m)	φ	κ (m ²)	saturation
Hot-airflow	1.80 × 10 ⁻⁴	8.85 × 10 ⁻¹²	-	-	-
Water	-	-	-	-	1
Solid	-	-	0.385	8.41 × 10 ⁻¹²	-

Source of hot-airflow: Saneewong Na Ayuttaya, S., Chakranond, C., Rattanadecho, P. and Kreewatcharin, T., (2012). Effect of Ground Arrangements on Swirling Flow in a Channel Subjected to Electrohydrodynamic Effects, ASME Journal of Fluids Engineering, 134, 051211-9.
Source of water sample and porous sample (water and solid): Sungsoontorn, S., Rattanadecho, P. and Pakdee, W. (2011). One-Dimensional Model of Heat and Mass Transports and Pressure Built Up in Unsaturated Porous Materials Subjected to Microwave Energy, Drying Technol., 29, 189–204.

Table 2
Thermal properties.

Modeling parameter	ρ(kg/m ³)	η(m ² /s)	k(W/m.K)	C _p (kJ/kg.K)
Hot-airflow	1.060	1.76 × 10 ⁻⁵	0.028	1.008
Water	998	1.005 × 10 ⁻⁵	0.588	4.186
Solid	2500	-	0.14	0.8

Source of hot-airflow: Saneewong Na Ayuttaya, S., Chakranond, C., Rattanadecho, P. and Kreewatcharin, T., (2012). Effect of Ground Arrangements on Swirling Flow in a Channel Subjected to Electrohydrodynamic Effects, ASME Journal of Fluids Engineering, 134, 051211-9.
Source of water sample and porous sample (water and solid): Sungsoontorn, S., Rattanadecho, P. and Pakdee, W. (2011). One-Dimensional Model of Heat and Mass Transports and Pressure Built Up in Unsaturated Porous Materials Subjected to Microwave Energy, Drying Technol., 29, 189–204.

3.1. Electric field analysis

The model is expressed to predict the electric field in a rectangular duct. To reduce the complexity of this problem, this study is based on the following assumptions:

- (1) The dielectric property is constant.
- (2) The effect of magnetic field is negligible.
- (3) The corona discharge occurs only in the vicinity around the electrode wire.

Electric field distribution is computed by using Maxwell's equations (Eqs. (1)–(4)) listed as below:

$$\nabla \cdot \epsilon \vec{E} = q, \tag{1}$$

$$\vec{E} = -\nabla V, \tag{2}$$

$$\nabla \cdot \vec{J} + \frac{\partial q}{\partial t} = 0, \tag{3}$$

$$\vec{J} = qb\vec{E} + q\vec{u}, \tag{4}$$

where E is electric field intensity and u is airflow velocity. Of which most of the corona current is collected at the tip of the electrode, charge density (Q) is calculated from Eq. (5):

$$V_0 = \frac{Q}{A\epsilon_0}d, \tag{5}$$

and

$$C = \frac{A\epsilon_0}{d}, \tag{6}$$

where V₀ and ε₀ are electrical voltage and dielectric permeability of free space at the tip of the electrode, respectively. Electricity capacity (C) is calculated from Eq. (6). Space charge density at the tip of the electrode (q₀) is described by Griffiths [29], as shown in Eq. (7). It is a concept in which excess electric charge is treated as a continuum of charge distributed over a region of space.

$$q_0 = \frac{Q}{V} = \frac{\epsilon_0 V_0}{hd}, \tag{7}$$

The governing equation for computing the electric force per unit volume (f_E) performing on fluid flow can be expressed by

$$\vec{f}_E = q\vec{E} - \frac{1}{2}\vec{E}^2\nabla\epsilon + \frac{1}{2}\nabla\left[\vec{E}^2\left[\frac{\partial\epsilon}{\partial\rho}\right]_{T}\rho\right], \tag{8}$$

From the right-hand side of Eq. (8), three terms are the electrophoretic, dielectrophoretic and electrostrictive forces, respectively. In the first term, the electrophoretic force or Coulomb force results from the net uncharged within the fluid or ions injected from the electrodes. Coulomb force results from the net charged fluid or ions injected from the electrodes. Electric field distribution is emitted from electrode wire and induces to the ground. The second term, the dielectrophoretic force is a consequence of inhomogeneity in the permittivity of the dielectric fluid due to the non-uniform electric field, temperature gradients, and phase differences. The last term, the electrostrictive force is caused by non-homogeneous electric field strength and the variation in dielectric constant with temperature and density [21]. From assumption, the dielectric properties are constant and homogeneity. Therefore, the second and third terms on the right-hand side of Eq. (8) are negligible. Consequently, Eq. (8) reduces to

$$\vec{f}_E = q\vec{E}, \tag{9}$$

Boundary and initial condition of the electric field is based on the following:

- (1) The outer sides of the boundary conditions are considered as zero

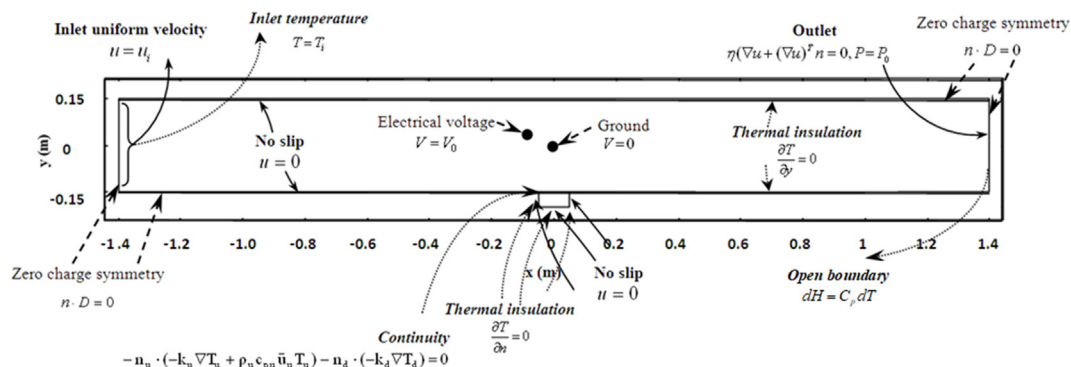


Fig. 2. Boundary conditions for analysis.

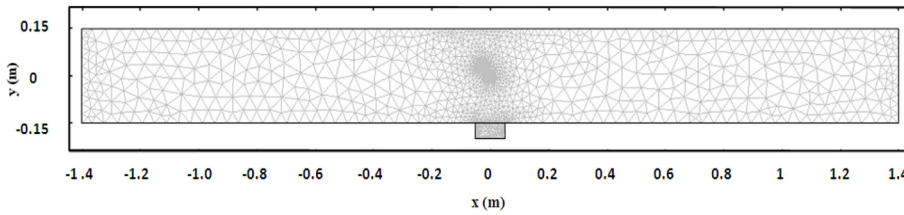


Fig. 3. A two-dimensional finite element meshes.

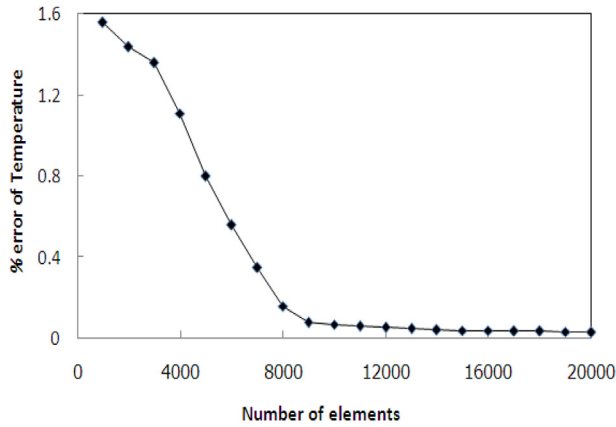


Fig. 4. Relationship between temperature change as a percentage and different number of elements from this study.

charge symmetry,

$$n \cdot D = 0, \tag{10}$$

(2) Electrode and ground are considered as electrical voltage and ground, respectively.

$$V = V_0, \text{ at electrode position} \tag{11}$$

$$V = 0, \text{ at ground position} \tag{12}$$

(3) The electrical voltage at the tip of the electrode (V_0) is fixed at 20 kV.

3.2. Flow field and heat transfer analysis in a rectangular duct

In order to simplify the problem, several assumptions have been offered into the flow and heat transfer analysis.

- (1) The effect of the phase change can be neglected.
- (2) The incompressible flow and the fluid physical properties are assumed to be constant.
- (3) The effect of buoyancy and emission or absorption of radiant energy is negligible.
- (4) The thermal properties of the fluid are considered to be constant.

The continuity and Navier–Stokes equations which coupled with Coulomb force equation are considered from Eqs. (13) and (14), respectively. They are expressed by:

$$\nabla \cdot \vec{u} = 0, \tag{13}$$

and

$$\rho \left[\frac{\partial \vec{u}}{\partial t} + (\vec{u} \cdot \nabla) \vec{u} \right] = -\nabla \vec{P} + \mu \nabla^2 \vec{u} + \vec{f}_E, \tag{14}$$

Temperature distribution in a rectangular duct from swirling flow is calculated by using energy equation, as shown in Eq. (15).

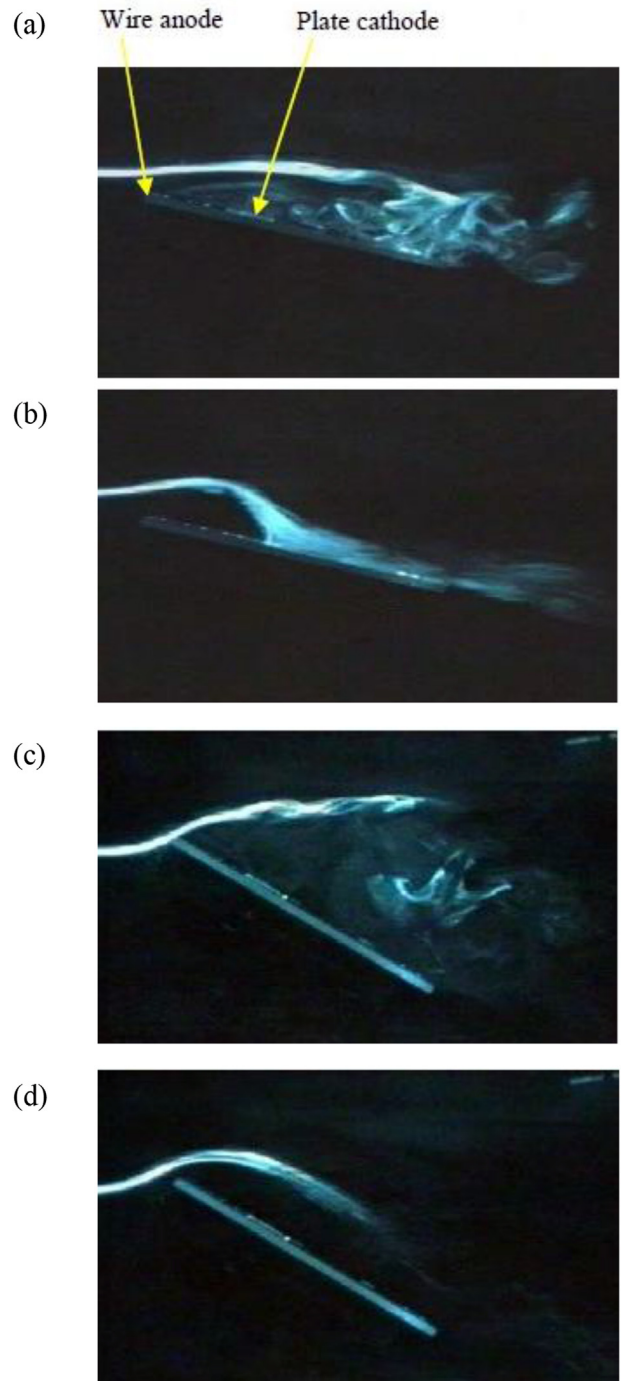


Fig. 5. The experimental flow visualization from Luc et al. [31] when $u_i = 0.35$ m/s: (a) No EHD when a flat plate at an angle of attack of 15° (b) $V_0 = 18$ kV when a flat plate at an angle of attack of 15° (c) No EHD when a flat plate at an angle of attack of 30° (d) $V_0 = 18$ kV when a flat plate at an angle of attack of 30° .

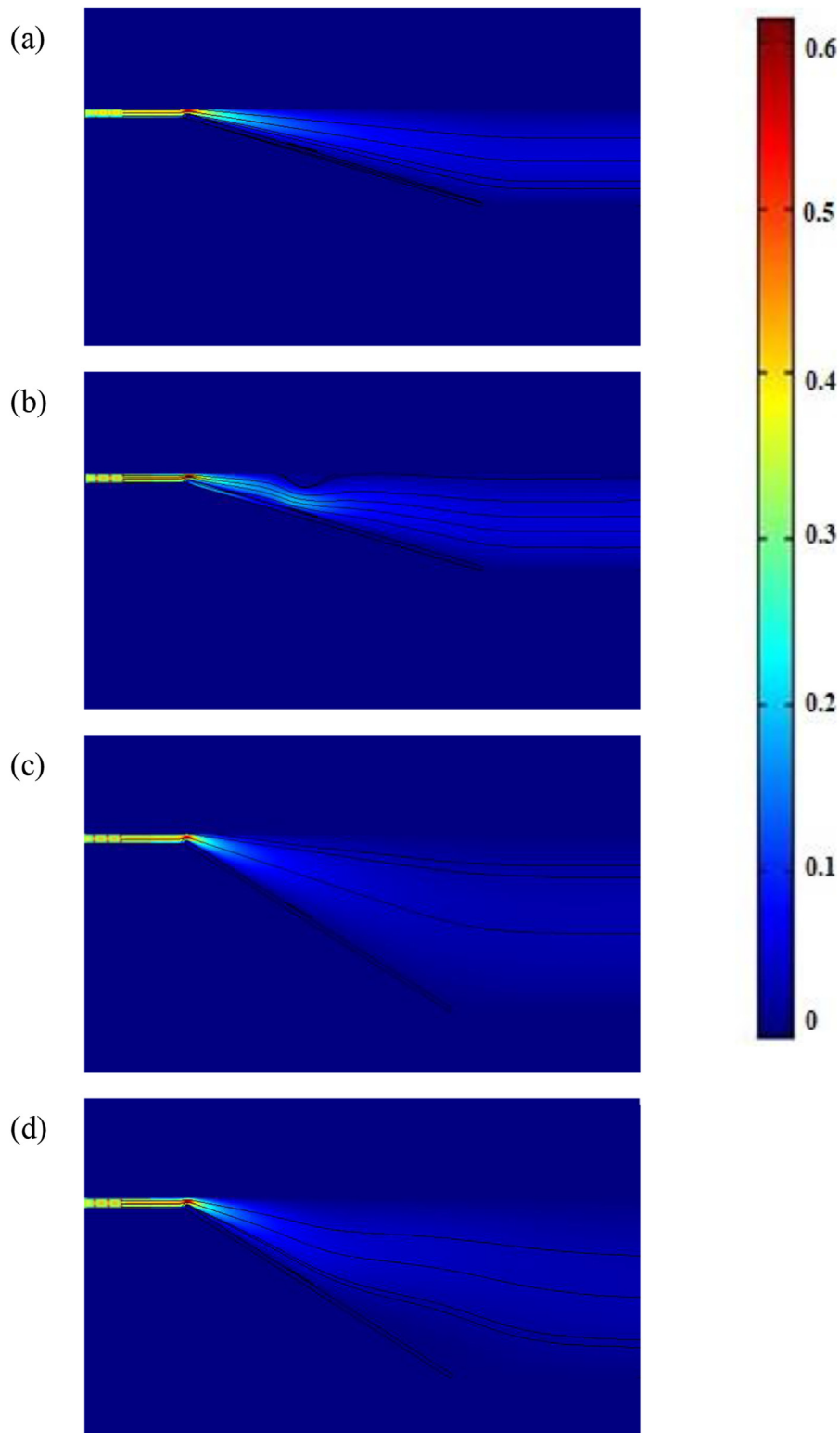


Fig. 6. Test results for validation purposes when $u_i = 0.35$ m/s: (a) No EHD when a flat plate at an angle of attack of 15° (b) $V_0 = 18$ kV when a flat plate at an angle of attack of 15° (c) No EHD when a flat plate at an angle of attack of 30° (d) $V_0 = 18$ kV when a flat plate at an angle of attack of 30° .

$$\rho C_p \left[\frac{\partial T}{\partial t} + \vec{u} \nabla T \right] = k(\nabla^2 T) \tag{15}$$

The Boundary condition of flow field and heat transfer is based on the following:

(1) The inlet velocity boundary condition of air is assumed to be

uniform. It is defined as:

$$\vec{u} = \vec{u}_i, \tag{16}$$

(2) The pressure of outlet boundary condition is considered with no viscous stress. This boundary condition specifies vanishing viscous stress along with a Dirichlet condition on the pressure:

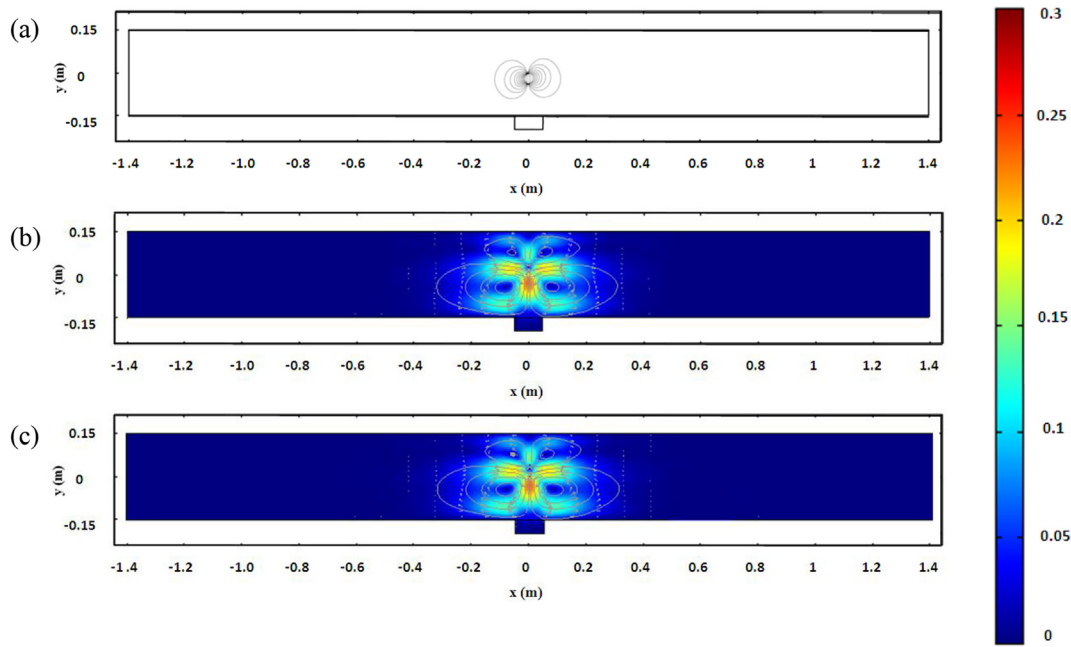


Fig. 7. Present simulated results along x-y plane in case of absent inlet airflow ($u_i = 0$ m/s) ($V_o = 20$ kV, $\theta = 90^\circ$ and $d = 4$ cm) (a) electric field (b) swirling flow and fluid flow within water sample and (c) swirling flow and fluid flow within porous sample.

$$\eta(\nabla \vec{u}) + (\nabla \vec{u})^T \cdot \vec{n} = 0 \text{ and } \vec{P} = \vec{P}_0, \tag{17}$$

(3) The upper and lower of rectangular ducts are considered as no-slip boundary condition, this is the standard and default boundary condition for a stationary solid wall. The condition prescribed:

$$\vec{u} = 0, \tag{18}$$

(4) To solve the temperature distribution, the inlet and outlet temperature boundary condition are shown in Eqs. (19) and (20), respectively, which defined as:

$$T = T(t_0), \tag{19}$$

and open boundary condition is defined at outlet boundary conditions *enthalpy change* = $dH = C_p dT$

$$\tag{20}$$

(5) The upper and lower walls of the rectangular duct are insulated, as shown in Eq. (21). The condition prescribed:

$$\frac{\partial T}{\partial y} = 0, \tag{21}$$

The initial condition of flow field and heat transfer is based on the following:

- (1) For Eq. (16), the inlet velocity of air (u_i) is 0.1 m/s.
- (2) For Eq. (19), the initial temperature of hot-airflow ($T(t_0)$) is 60 °C.

3.3. Fluid flow and heat transfer analysis within a sample

The governing equations describing the flow field and heat transfer within the porous sample is calculated from Eqs. (22) and (23). They are expressed by Keangin and Rattanadecho [30]:

$$\frac{1}{\varphi} \frac{\partial \vec{u}}{\partial t} + \frac{1}{\varphi^2} (\vec{u} \cdot \nabla) \vec{u} = -\frac{1}{\rho_l} \nabla P + \frac{\mu}{\rho \varphi} \nabla^2 \vec{u} - \frac{\mu \vec{u}}{\rho \kappa}, \tag{22}$$

and

$$(\rho C_p)_{\text{eff}} \frac{\partial T}{\partial t} + (\rho C_p)_l \vec{u} \cdot \nabla T = k_{\text{eff}} \nabla^2 T, \tag{23}$$

where φ is porosity, κ is permeability and effective thermal conductivity (k_{eff}) in a porous sample is computed from

$$k_{\text{eff}} = (1 - \varphi)k_s + \varphi k_l, \tag{24}$$

and

$$(\rho C_p)_{\text{eff}} = (1 - \varphi)(\rho C_p)_s + \varphi (\rho C_p)_l, \tag{25}$$

Subscript s and l are the solid and liquid phase, respectively. Nevertheless, the governing equations describing the flow field and heat transfer within the water sample is calculated from Eqs.(13)–(15), but the properties of water are considered instead of air. By Eq. (14) is not considered electric force.

The boundary and the initial condition of flow field and heat transfer within a sample are based on the following:

- (1) The only upper surface of the sample is exposed to hot-airflow which describes in Eq. (28). The other boundary conditions of flow field and heat transfer are considered as no-slip boundary condition (Eq. (26)), and insulated boundary condition (Eq. (27)), respectively.

$$\vec{u} = 0, \tag{26}$$

and

$$\frac{\partial T}{\partial n} = 0, \tag{27}$$

- (2) The initial within sample is zero and the initial temperature within water sample and porous ($T_s(t_0)$) is 20 °C.

3.4. Interface of hot-airflow and samples (water sample and porous sample)

It is evident that a generalized conjugate approach to the combined fluid flow and heat transfer process, the interface of hot-air and sample is solved by using Eq. (28). It is defined as

$$-n_u \cdot (-k_u \nabla T_u + \rho_u c_{p,u} \vec{u}_u T_u) - n_d \cdot (-k_d \nabla T_d) = 0. \tag{28}$$

The upper and the lower interfaces are designated by subscript u and d , respectively.

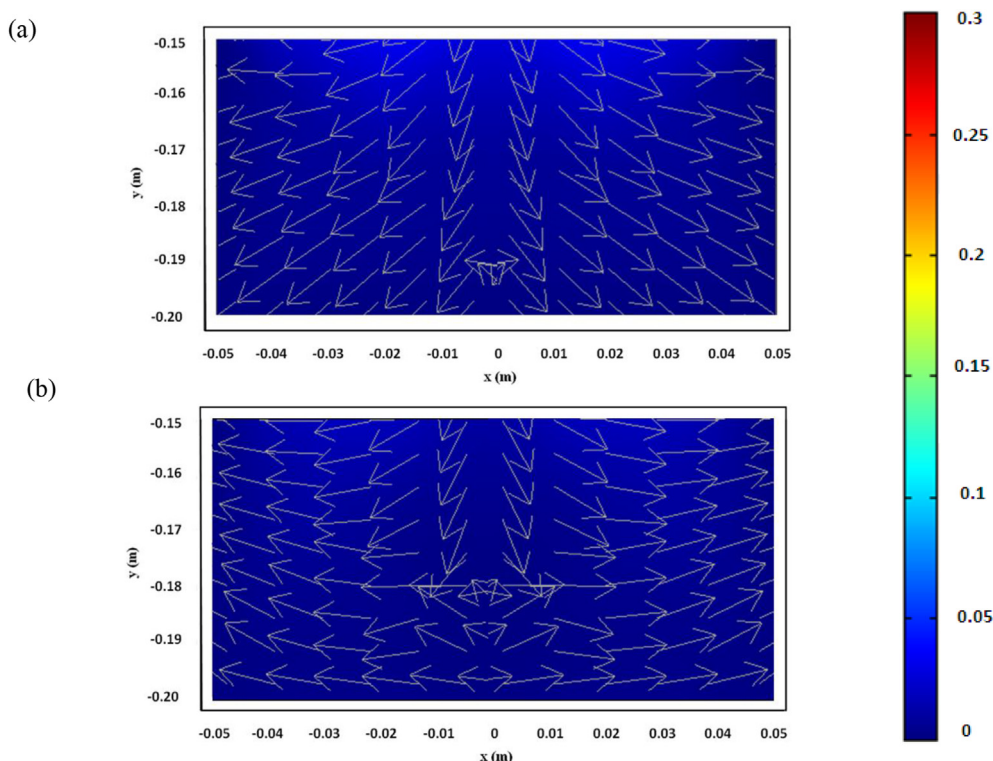


Fig. 8. Present simulated results along x-y plane in case of absent inlet airflow ($u_i = 0$ m/s) ($V_0 = 20$ kV, $\theta = 90^\circ$ and $d = 4$ cm) (a) fluid flow within water sample and (b) fluid flow within porous sample.

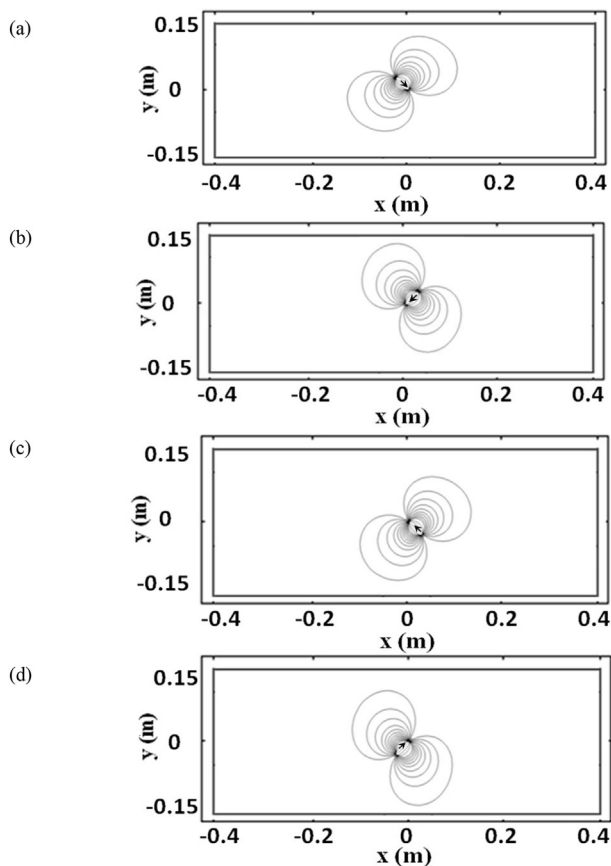


Fig. 9. Electric field in various θ ($V_0 = 20$ kV and $d = 4$ cm): (a) $\theta = 45^\circ$ (b) $\theta = 135^\circ$ (c) $\theta = 225^\circ$ and (d) $\theta = 315^\circ$.

4. Calculation procedure

The COMSOL Multiphysics is the software for using in this research paper. It is the platform for physics-based modeling and simulation. It is a general-purpose software platform, based on advanced numerical methods, for modeling and simulating physics-based problems. COMSOL Multiphysics will be able to account for coupled or multiphysics phenomena. It can further expand the simulation platform with dedicated physics interfaces and tools for electrical, mechanical, fluid flow, and chemical applications. The finite element method using a collocation method is used to analyze the transient problems and compute a swirling flow by EHD technique. In order to obtain a good approximation, a fine mesh is specified in the sensitive areas. This study provides a variable mesh method for solving the problem as shown in Fig. 3. The two-dimensional model is discretized using triangular elements and the Lagrange quadratic is then used to approximate the electric, flow and temperature field across each element. The convergence test is carried out to identify the suitable number of elements required. The relationship between temperature change as a percentage and the different number of elements is shown in Fig. 4. It is the convergence curve resulting from the convergence test. The high electrical voltage (V_0) is applied at 20 kV. Temperature and average velocity of inlet hot-airflow are controlled at 60°C and 0.1 m/s, respectively. The relationship between temperature change as the percentage and different elements from simulations at a critically sensitive point is showed, interface area between lower wall of a rectangular duct and upper surface of the water sample is considered based on conjugate approach. This convergence test leads to the mesh with approximately 9000 elements. It is reasonable to assume that, at this element number, the accuracy of the simulation results is independent of the number of elements.

5. Model verification

To verify the accuracy of flow patterns, the resulting data is

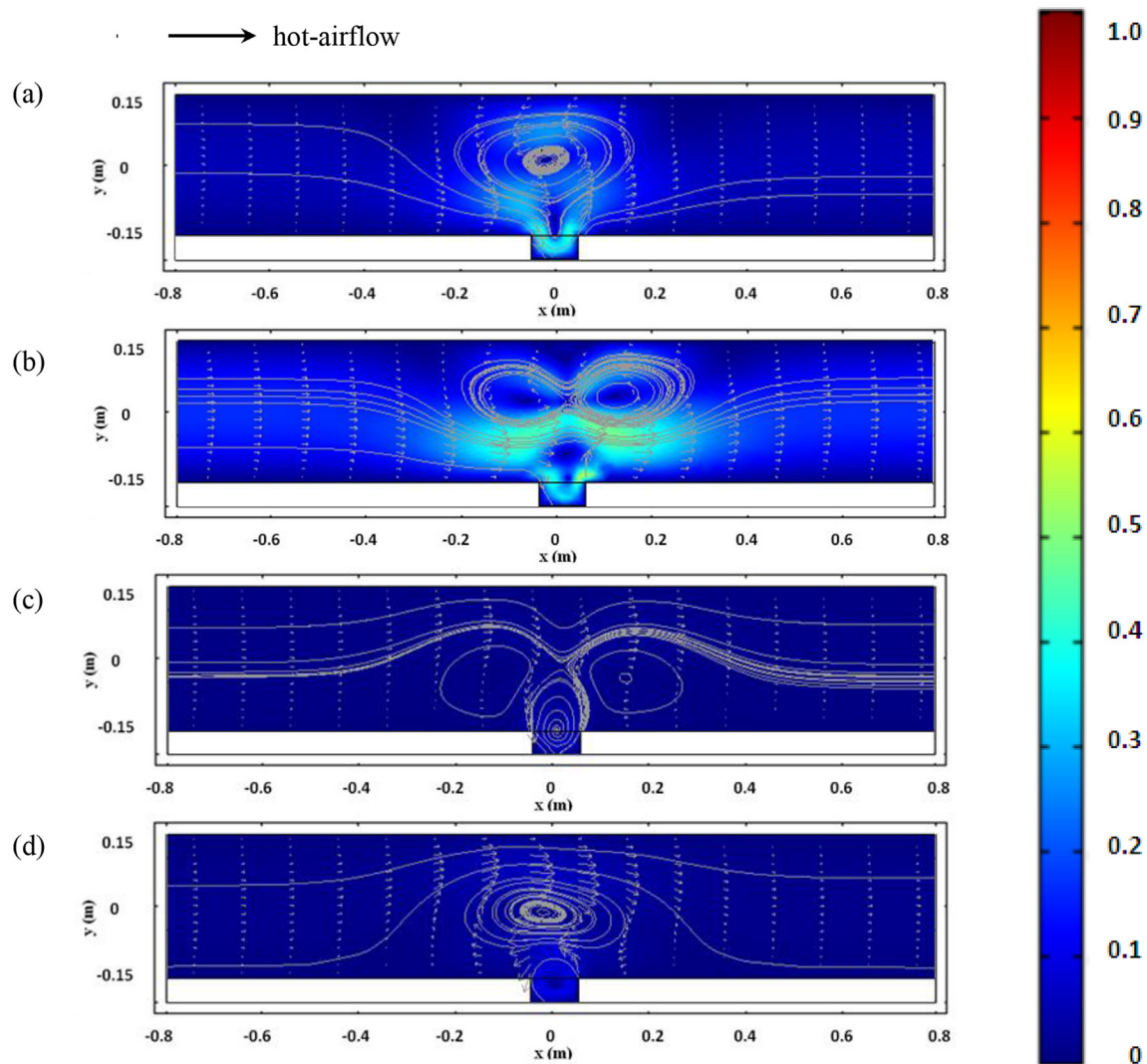


Fig. 10. Swirling flow and fluid flow within water sample in various θ ($V_0 = 20$ kV and $d = 4$ cm): (a) $\theta = 45^\circ$ (b) $\theta = 135^\circ$ (c) $\theta = 225^\circ$ and (d) $\theta = 315^\circ$.

validated against the experimental flow visualization from Luc et al. [31] when $u_i = 0.35$ m/s, as shown in Fig. 5. For experimental setup, airflow ($u_i = 0.35$ m/s) is moved from the left to the right direction and the airflow around the inclined plate is visualized with an oil smoke filament lightened by the 2d laser sheet. In case of no EHD, an inclined plate at an angle of attack of 15° and 30° are shown in Fig. 5(a) and (c), respectively. When airstream flows without the electric field, it separates from the inclined plate. In case of EHD ($V_0 = 18$ kV), the inclined plate at an angle of attack of 15° and 30° are shown in Fig. 5(b) and (d). The electrode and ground are made of copper and aluminum, respectively. For low angle (Fig. 5(b)), the airflow remains attached to the inclined plate. For higher angle (Fig. 5(d)), the airflow is reattached and the wake highly decreases. The test result for validation purpose is visualized in Fig. 6. The finite element method using a collocation method is used to analyze the validated problems. In case of no EHD and $u_i = 0.35$ m/s, the trend of flow visualization of an inclined plate at an angle of attack of 30° (Fig. 6(c)) is more separated than an inclined plate at an angle of attack of 15° (Fig. 6(a)). In case of EHD and $u_i = 0.35$ m/s, the trend of flow visualization of an inclined plate at an angle of attack of 15° (Fig. 6(b)) is more reattached than an inclined

plate at an angle of attack of 30° (Fig. 6(d)). In this result, electric discharge is to convert electrical energy into kinetic energy inside the boundary layer in order to accelerate the flow close to the inclined plate. In addition, the flow visualization by oil incense technique and simulation has a good agreement.

6. Results and discussion

The mathematical model combined with Coulomb force, energy, continuity and incompressible Navier-Stokes equation are systematically proposed. The coupled models of the swirling flow by electric field effect and unsteady heat transfer as well as the boundary conditions are solved numerically on EHD technique with the conjugate approach.

6.1. Swirling flow in case of absent inlet airflow

For absent inlet airflow ($u_i = 0$ m/s), the effect of electric field influences with swirling flow is presented. From Fig. 1, the electrical voltage (V_0), the angle between electrode and ground (θ) and

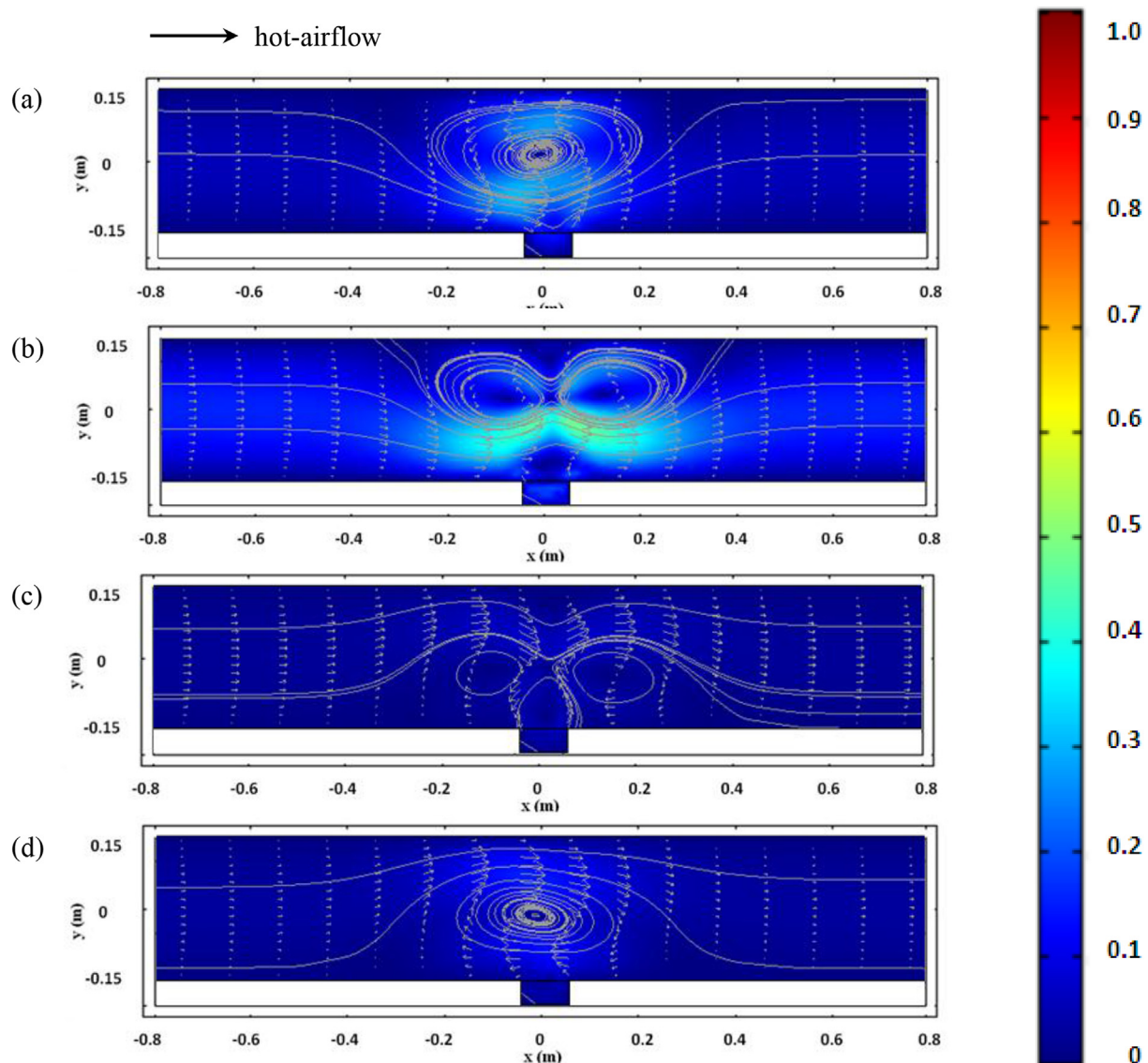


Fig. 11. Swirling flow and fluid flow within porous sample in various θ ($V_0 = 20$ kV and $d = 4$ cm): (a) $\theta = 45^\circ$ (b) $\theta = 135^\circ$ (c) $\theta = 225^\circ$ and (d) $\theta = 315^\circ$.

displacement between electrode and ground (d) are 20 kV, 90° and 4 cm, respectively. The electric field effect, shear flow from charged airflow is induced so uncharged airflow around the area has appeared. This causes the shear flow to become the swirling flow. Furthermore, electric field direction is influenced the swirling flow pattern. Fig. 7 shows the simulated results of electric field pattern (Fig. 7(a)) and swirling flow pattern (Fig. 7(b–c)) of air along x - y plane. It can be seen that electric field from Fig. 7(a) moves from electrode to the ground and it concentrates between electrode and ground area. By Fig. 7(b) and (c) show swirling flow in a rectangular duct and fluid flow within water sample and porous sample, respectively. From shear flow effect, four cells of swirling flow have appeared in the rectangular duct. The big front cell and big latter cell are appeared in clockwise and counter-clockwise direction, respectively. The big double cells of swirling flow are induced by shear flow so the small doubles cells are swirled. Due to electrical voltage (V_0), the angle between electrode and ground (θ) and displacement between electrode and ground (d) do not difference so characteristic of swirling flow in the rectangular ducts are the same

pattern. Within the sample, the interface between hot-airflow and sample is investigated by the concept of conjugate approach, it can be seen that fluid flow is supported by swirling flow, as shown in Fig. 8. By average, the velocity of fluid flow within the water sample (Fig. 8(a)) is higher than within the porous sample (Fig. 8(b)). Fluid flow can move rapidly through the bottom of water sample container. However, fluid flow can move partially through the porous sample. This is due to the permeability of porous medium (κ) has strong effect on the fluid flow within the porous sample. The presence of porous matrix, i.e., glass beads that resist the flow motion of the liquid in the voids. Nevertheless, the conduction heating mode is still higher in case of the porous sample since it displays a higher effective thermal conductivity as compared to the water sample. Furthermore, it can be seen that both of electric field and swirling flow have appeared between electrode and the ground area, so shear flow is locally concentrated when ground is investigated. For the next Figures show electric field and swirling flow in x - y plane which focuses to the plane of electrode and ground area.

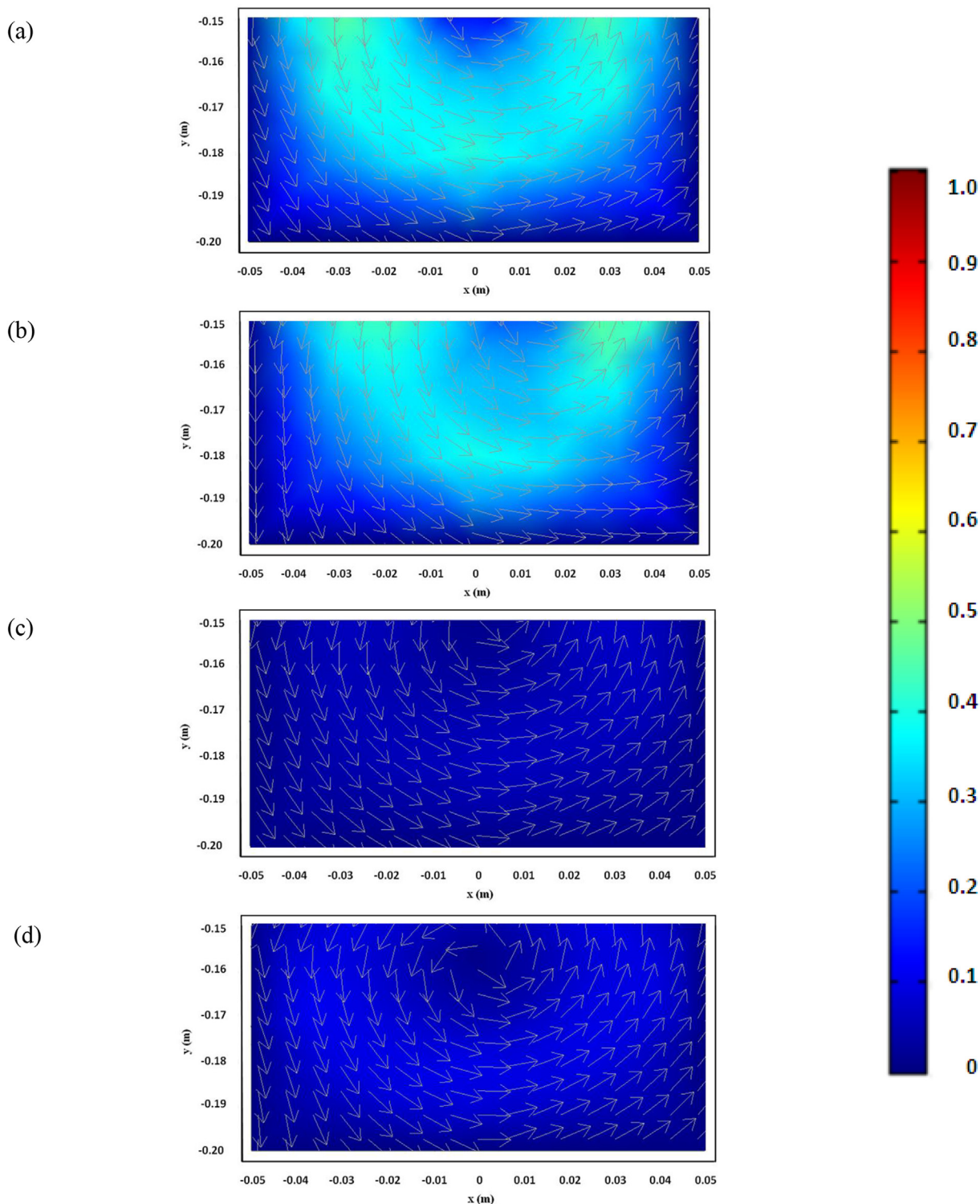


Fig. 12. Fluid flow within water sample in various θ ($V_0 = 20$ kV and $d = 4$ cm): (a) $\theta = 45^\circ$ (b) $\theta = 135^\circ$ (c) $\theta = 225^\circ$ and (d) $\theta = 315^\circ$.

6.2. Swirling flow when using various electrode arrangements

In order to compare the effect of electrode arrangements, the angle between electrode and ground (θ) are varied from 0 to 360° in the clockwise direction. From Fig. 1, the electrical voltage (V_0), uniform

inlet velocity (u_i) and displacement between electrode and ground (d) are 20 kV, 0.1 m/s and, 4 cm, respectively. Fig. 9 shows electric field distribution in the various angle between electrode and ground (θ), Fig. 9(a–d) are $\theta = 45^\circ, 135^\circ, 225^\circ$ and 315° , respectively. An electric field is the force field that is the property of one electric charge that will

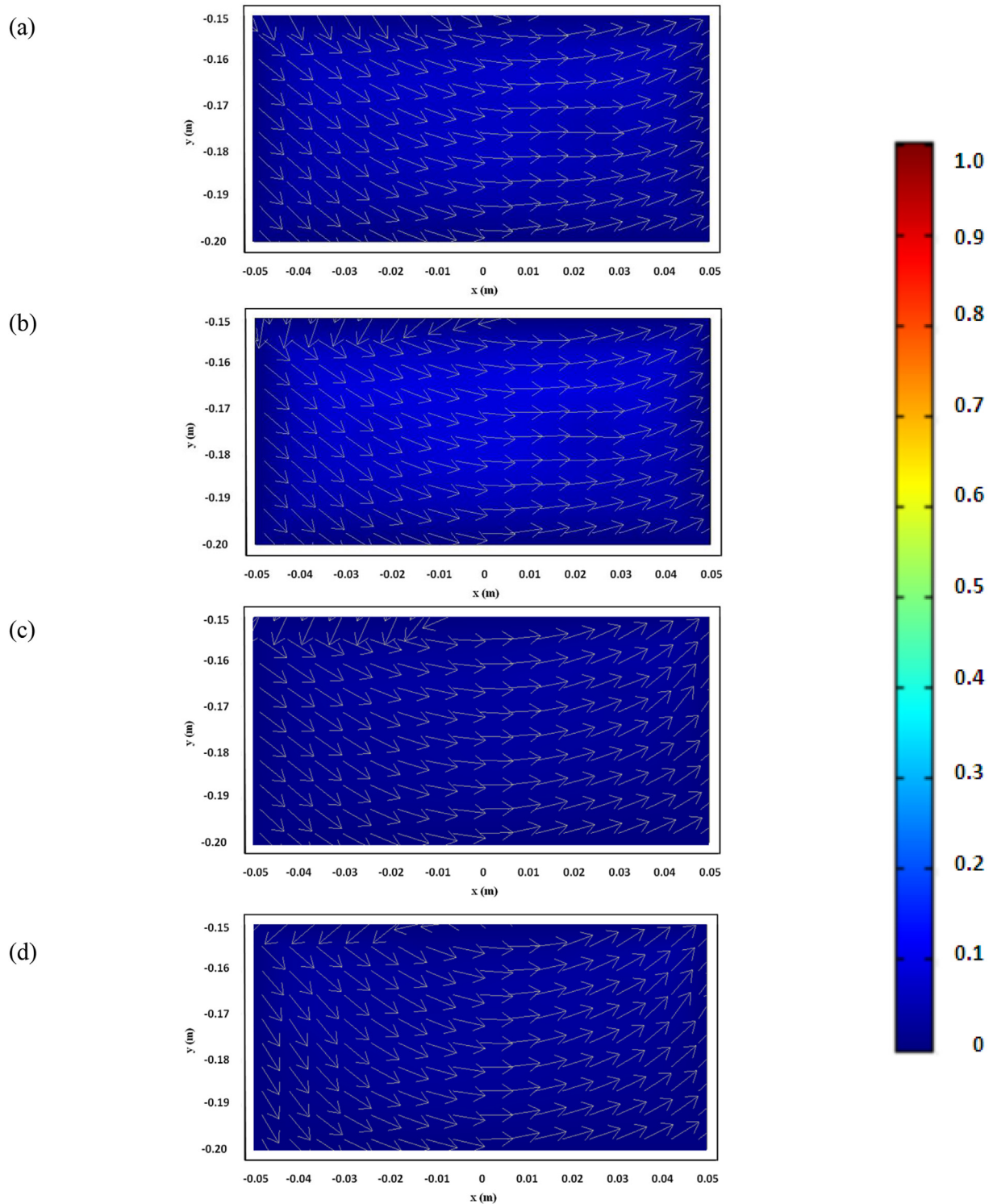


Fig. 13. Fluid flow within porous sample in various θ ($V_0 = 20$ kV and $d = 4$ cm): (a) $\theta = 45^\circ$ (b) $\theta = 135^\circ$ (c) $\theta = 225^\circ$ and (d) $\theta = 315^\circ$.

affect the second charge by repelling or attracting that second charge. The direction of electric field is taken to be the direction of the force. The electric field is radially outward from the electrode and radially inward toward ground. In all cases, the electric field moves outwardly from electrode to ground and concentrate at both electrode and ground. The

primary flow from electric field moves from electrode to ground in order to induce the shear flow. This causes the shear flow to become the swirling flow or secondary flow. Due to electrical voltage is not differenced, so electric field intensity is not differenced. It is noted that electrical field from Eq. (2) has a trend corresponding to that of electric

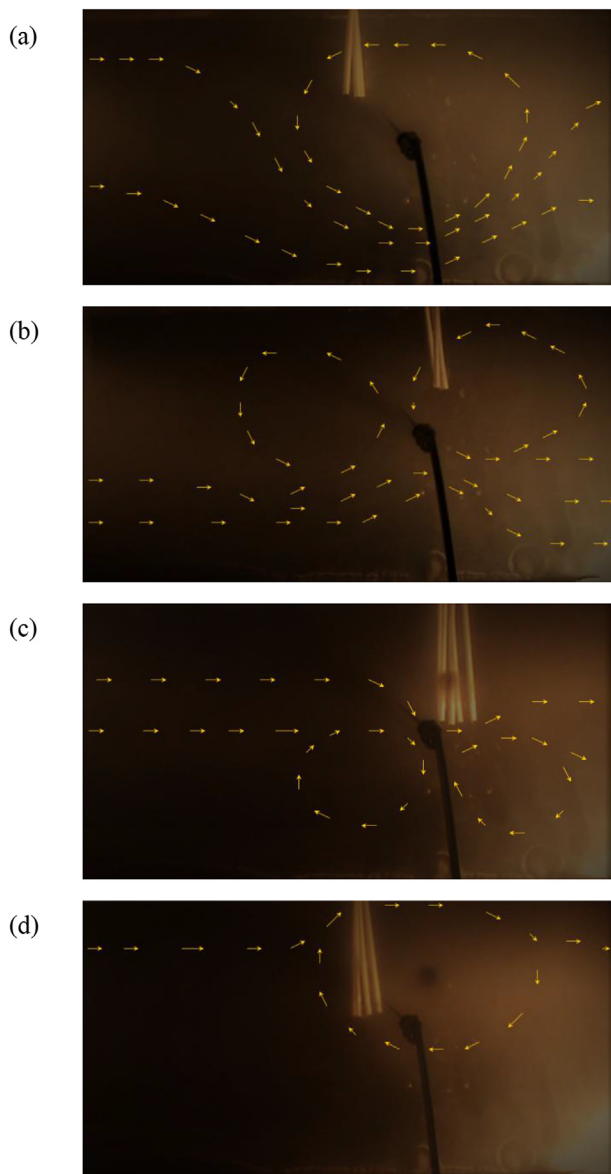


Fig. 14. Flow visualization in various θ : (a) $\theta = 45^\circ$ (b) $\theta = 135^\circ$ (c) $\theta = 225^\circ$ and (d) $\theta = 315^\circ$.

force from Eq. (9). Furthermore, space charge density is the same direction with the electric field. When electric field induced hot-airflow, it can be seen that electric field from various angles can induce the differentiation of swirling flow pattern. The swirling flow of airflow with the water sample and porous sample are considered from Figs. 10 and 11, respectively. When considering in a rectangular duct, position and vortex strength depends on the location of electrode respecting with the ground position. When $\theta = 0^\circ$ and $\theta = 180^\circ$, electrode and ground is stalled in the same direction of the hot-airflow. So the effect of shear flow is not strong, the velocity of charged and uncharged airflow is little difference to the small swirling flow has appeared. From $\theta = 45^\circ$ (Figs. 10(a) and Fig. 11(a)) and $\theta = 90^\circ$, the swirling flow motion displays in the counterclockwise direction. By the arrangement of $\theta = 90^\circ$ is supported from the inlet airflow, so $\theta = 90^\circ$ is widely swirled and extended more than that of $\theta = 45^\circ$. Due to shear flow effect, double cells are swirled for the different direction, as shown in θ

$= 135^\circ$ (Figs. 10(b) and Fig. 11(b)) and $\theta = 225^\circ$ (Figs. 10(c) and Fig. 11(c)). As $\theta = 135^\circ$, the front cell and latter cell are swirled in the counterclockwise direction, but two cells of swirling flow from $\theta = 225^\circ$ are appeared in the different direction, the front cell and latter cell are swirled in the clockwise direction. Due to electrode arrangements are installed in the different direction. From $\theta = 270^\circ$ and $\theta = 315^\circ$ (Figs. 10(d) and Fig. 11(d)), the swirling flow is circulated in the clockwise direction when inlet airflow is supplied from the left to the right direction. Due to the angle between electrode and ground are varied, it can be seen that the differences of swirling flow appear in other patterns. This is because electric field induction hot-airflow induces shear flow in the different direction. By the maximum velocity is appeared in case of $\theta = 90^\circ$. So $\theta = 90^\circ$ is optimum electrode position due to it can induce the suitable electric force. From Figs. 12 and 13, the swirling flow pattern in a rectangular duct is no different when the angle between electrode and ground is not varied. This is because swirling flow is depended on shear flow effect. In case of control an angle, electric field can induce the same of swirling flow pattern.

Based on the concept of conjugate transport phenomena analysis, swirling flow and fluid flow by EHD technique have been investigated within a specified domain. Figs. 12 and 13 show fluid flow within the water sample and porous sample, respectively. In case of water sample (Fig. 12), the single phase of water is considered. Fluid flow within the sample from various angles is depended on the swirling flow direction and hot-airflow direction. From Fig. 1, the angle between electrode and ground (θ) is varied in clockwise direction from 0 to 360° and the displacement between electrode and ground is $d = 4$ cm. The disturbance of swirling flow between interface zones is related with increasing of velocity within the water sample. From Fig. 12(a–b), position of swirling flow is strongly disturbed between interface zones so fluid flow within the water sample is clearly increased the velocity. By Fig. 12(c–d), swirling flow is not supported by the shear flow so fluid flow within the water sample is slowly increased the velocity. In case of the porous sample (Fig. 13(a–d)), two phases of solid and water are considered and are in saturated condition. The void fraction is defined as the fraction of the flow-channel volume that is occupied by the liquid phase (water) or, alternatively, as the fraction of the cross-sectional area of the channel that is occupied by the liquid phase. In this study, water saturation void fraction is 1. Due to the density of porous is higher than the density of water and permeability (κ) is the property of the porous material that is an indication of the ability for fluids (gas or liquid) to flow through the porous material. Namely, having the porous matrix which will retard the fluid flow. So in all cases, the velocity of fluid flow of porous sample is lower than water sample. From above data, within the sample is appeared for two terms. The first and the second terms are conduction and natural convection, respectively. In this study, sample properties are the main mechanism of the natural convection, it is a mechanism, or type of heat transport, in which the fluid motion but only by density differences in the fluid occurring due to temperature gradients.

6.3. Motion of airflow

In order to confirm the accuracy of the present numerical model, the modified case of the simulated results is validated against the experimental data. From experimental setup in this study, flow visualization has appeared from incense smoke technique. The hot-airflow is supplied from a blower an electric heater. In order to control the temperature of the hot air, a thermocouple sensor (TC) is placed in front of the test section, where the cross-sectional area is 30×30 cm. The high voltage power supply (ACOPIAN model: NO30HP2M.-230) is used to create electrical voltage. A copper electrode wire is suspended from the

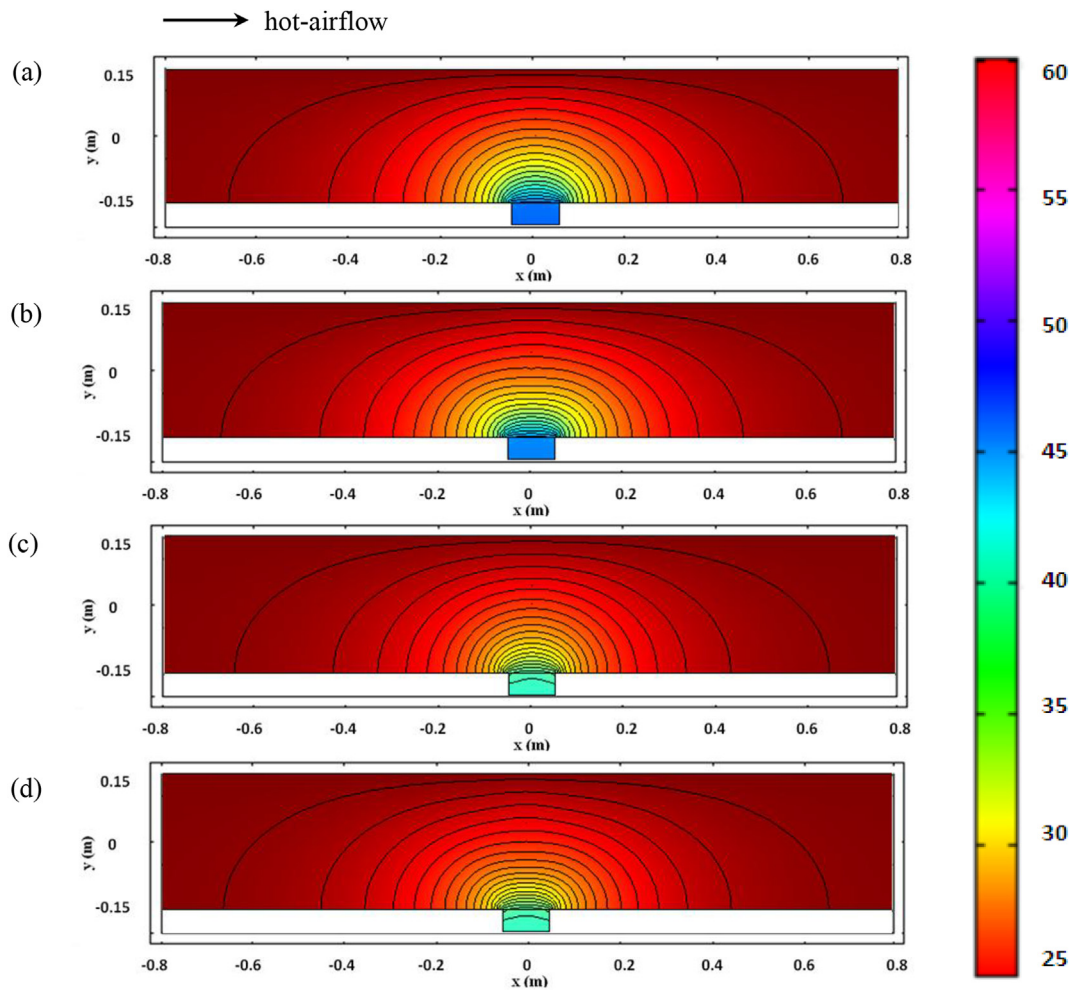


Fig. 15. Temperature distributions for 250 s and $u_i = 0$ m/s (a) No EHD within water sample (b) EHD within water sample ($V_0 = 20$ kV, $\theta = 90^\circ$ and $d = 4$ cm) (c) No EHD within porous sample (d) EHD within porous sample ($V_0 = 20$ kV, $\theta = 90^\circ$ and $d = 4$ cm).

top of rectangular duct and it is placed in the front of the packed bed and a copper ground is suspended horizontally across the test section. In order to observe the motion of airflow subjected to the electric field, incense smoke technique is used from smoke generator (GUNT HAMBURG: HM 170.52). A spotlight of 500 W is placed at the outlet of rectangular duct flow and the light direction is opposite to the flow direction. The inlet velocity is 0.1 m/s and the electrical voltage is 20 kV. The motion of airflow is continuously captured by a digital video camera record (SONY: VCT-R640). The primary flow from electric field moves from electrode to ground in order to induce the shear flow. This causes the shear flow to become the swirling flow or secondary flow. In various angles between electrode and ground (θ), it can induce the differentiation of swirling flow pattern, as shown in Fig. 14. When $\theta = 45^\circ$ (Fig. 14(a)), the swirling flow motion displays in the counterclockwise direction due to shear flow effect. The double cells are swirled in the different direction, as shown in $\theta = 135^\circ$ (Fig. 14(b)). The front cell and latter cell are swirled in the counterclockwise direction, respectively, but two cells of swirling flow from $\theta = 225^\circ$ (Fig. 14(c)) are appeared in the different direction. Due to electrode arrangements are installed in the different direction. From $\theta = 315^\circ$ (Fig. 14(d)), the swirling flow is circulated in the clockwise direction when inlet airflow is supplied from the left to the right direction. It can be seen that similar trend between incense smoke technique and

numerical modeling of swirling flow. By trend of swirling flow from $\theta = 45^\circ$ (Figs. 10 and 11(a)), $\theta = 135^\circ$ (Figs. 10 and 11(b)), $\theta = 225^\circ$ (Figs. 10 and 11(c)) and $\theta = 315^\circ$ (Figs. 10 and 11(d)) are similar with trend of swirling flow from $\theta = 45^\circ$ (Fig. 14(a)), $\theta = 135^\circ$ (Fig. 14(b)), $\theta = 225^\circ$ (Fig. 14(c)) and $\theta = 315^\circ$ (Fig. 14(d)). It is shown that the comparison results in both techniques are in good agreement. These confirm the accuracy of the present numerical model. In addition, the arrangement of $\theta = 45^\circ$ is supported from the inlet airflow, so the swirling flow is clearly swirled and concentrated more than the other cases.

6.4. Heat transfer in case of No EHD and EHD effect

From Fig. 15, swirling flow and temperature distributions for 250 s in case of No EHD and EHD are compared when absent inlet airflow ($u_i = 0$ m/s). In case of No EHD (Fig. 15(a) and (c)), swirling flow does not appear so temperature distribution is not frantically. In case of EHD (Fig. 15(b) and (d)), the electrical voltage (V_0), the angle between electrode and ground (θ) and displacement between electrode and ground (d) are 20 kV, 90° and 4 cm, respectively, as shown in Fig. 1. The swirling flow from Fig. 7(b) and (c) are affected by the temperature distribution of water sample (Fig. 15(b)) and porous sample (Fig. 15(d)), respectively. The swirling flow is influenced by heat

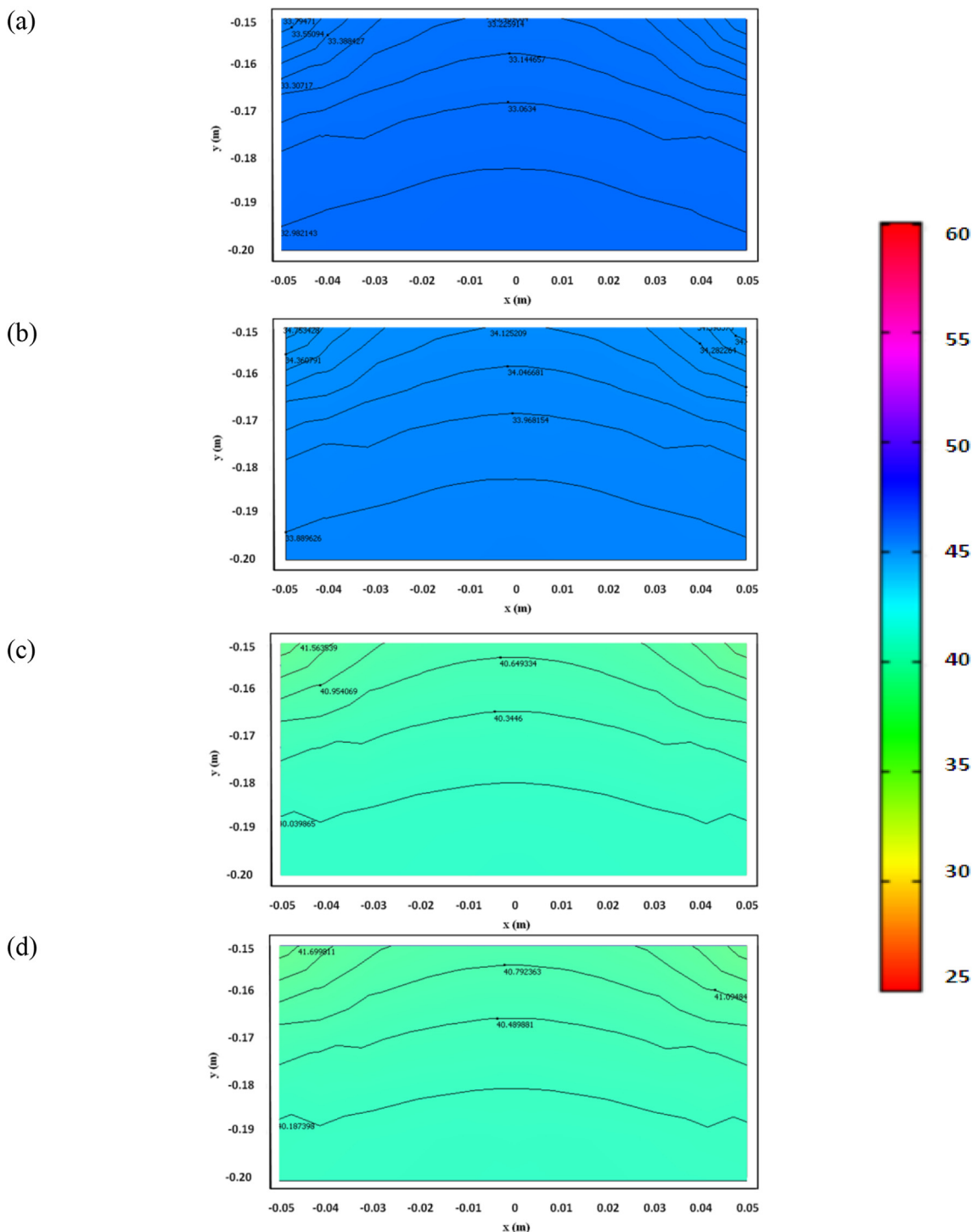


Fig. 16. Temperature distribution within sample for 250 s and $u_i = 0$ m/s (a) No EHD within water sample (b) EHD within water sample when $V_0 = 20$ kV, $\theta = 90^\circ$ and $d = 4$ cm (c) No EHD within porous sample (d) EHD within porous sample when $V_0 = 20$ kV, $\theta = 90^\circ$ and $d = 4$ cm.

transfer so temperature distribution is spreader over the sample. Fig. 16 shows temperature distribution within the sample for 250 s and absent inlet airflow. Heating zone of water sample in case of EHD (Fig. 16(b)) is higher than in case of No EHD (Fig. 16(a)) and heating zone of porous sample in case of EHD (Fig. 16(d)) is higher than in case of No EHD (Fig. 16(c)). So temperature distribution of the sample in case of EHD is

clearly increased but in case of No EHD, the temperature distribution of the sample is slowly increased. It can be seen that besides the shear flow effect, swirling flow is affected by temperature distribution so it affects the sample. In addition, the heating zone within the porous sample (Fig. 16(c-d)) is higher than within water sample (Fig. 16(a-b)), due to the difference of sample properties. By specific heat capacity of glass

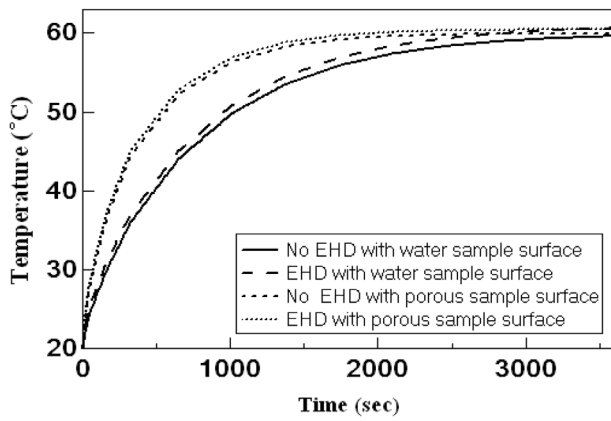


Fig. 17. Comparison of sample surface temperature for cases of No EHD and EHD ($V_0 = 20$ kV, $\theta = 90^\circ$ and $d = 4$ cm) within water sample and within porous sample.

beads or porous sample is lower than the specific heat capacity of the water sample. When the temperature of the sample surface is considered, variations of temperatures are treated by parabolic function as shown in Fig. 17. By trend of temperature in case of the porous sample is steeper than that in case of the water sample. So sample properties are influenced by sample surface temperature.

6.5. Heat transfer when various electrode arrangements

In this section, flow velocity and heat transfer area are increased when improvement of thermal efficiency. From the initial time ($t = 0$ s), temperature in a rectangular duct is 60°C and temperature within sample is 20°C . After time progress, the temperatures within sample are increased with increasing times. Interface between hot-

airflow and sample is investigated by the concept of conjugate approach. The swirling flow can clearly disturb the temperature in the rectangular duct, heat from airflow transfers to the sample so the temperature of airflow decreases. When temperature of sample closes to temperature of airflow, rate of heat transfer becomes lower. This causes temperature at the sample surface gradually increases. As shown in Fig. 18, temperature distribution in a rectangular duct and within water sample is presented. For No EHD case, the uniform inlet velocity (u_i) is 0.1 m/s. For EHD case, the electrical voltage (V_0), uniform inlet velocity (u_i), angle between electrode and ground (θ) and displacement between electrode and ground (d) are 20 kV, 0.1 m/s, 30° and 4 cm, respectively, as shown in Fig. 1. When time = 900 s, temperature distribution of No EHD case is supported with only hot-airflow so within water sample is slowly increased. But within water sample in case of EHD is clearly increased due to besides the shear flow effect, swirling flow is affected with temperature distribution so it affects within the water sample. Heating zone within water sample in case of EHD (Fig. 18(b)) is higher than within water sample in case of No EHD (Fig. 18(a)). From Figs. 19 and 20 show temperature distribution in various θ . When $t = 900$ s, temperature distribution in a rectangular duct and within sample are presented. From Fig. 1, the electrical voltage (V_0), uniform inlet velocity (u_i) and displacement between electrode and ground (d) are 20 kV, 0.1 m/s and 4 cm, respectively. When consider within the water sample (Fig. 19), swirling flow in the rectangular duct from Fig. 10 can induced fluid flow within water sample (Fig. 12) and it can attract heat at water sample surface so temperature within water sample is increased. From Fig. 12(a–b), fluid flow within the water sample is clearly increased the velocity so temperature distribution within the water sample (Fig. 19(a–b)) is rapidly increased. It can be seen that heating zone is perturbed by swirling flow. In the all cases, heat at 60°C is transferred from left to right direction and heat becomes lower when heat moves across the sample surface. Furthermore, temperature distribution at sample surface area is affected within sample. With swirling flow effect, fluid flow above the sample surface moves faster and then leads the

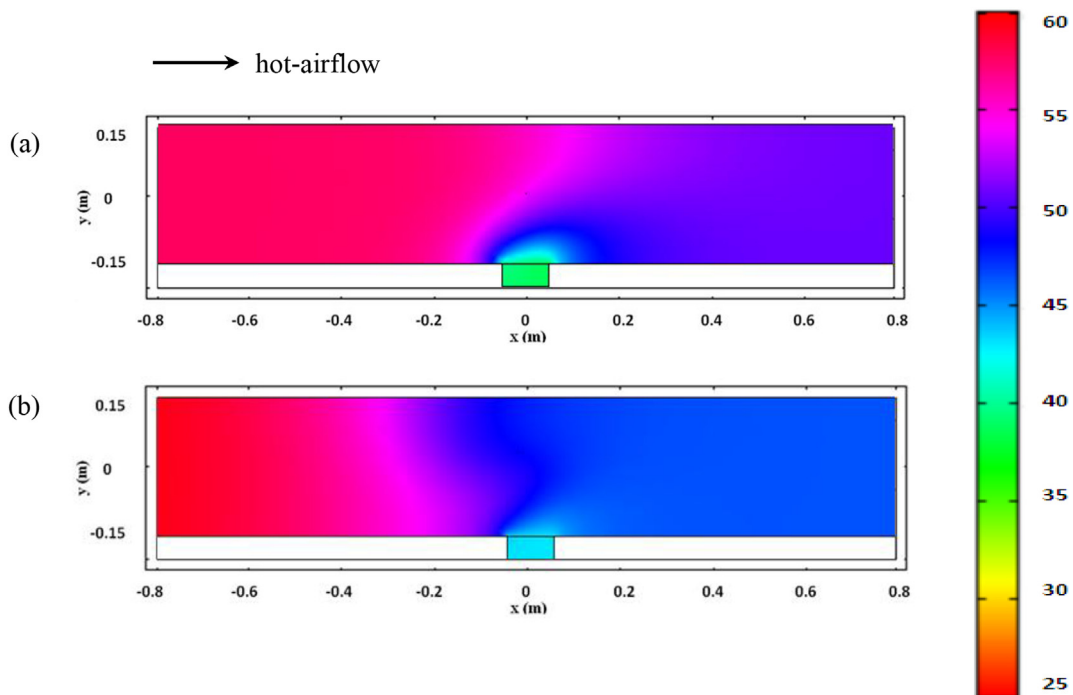


Fig. 18. Temperature distribution for 900 s within water sample (a) No EHD (b) EHD ($V_0 = 20$ kV, $\theta = 30^\circ$ and $d = 4$ cm).

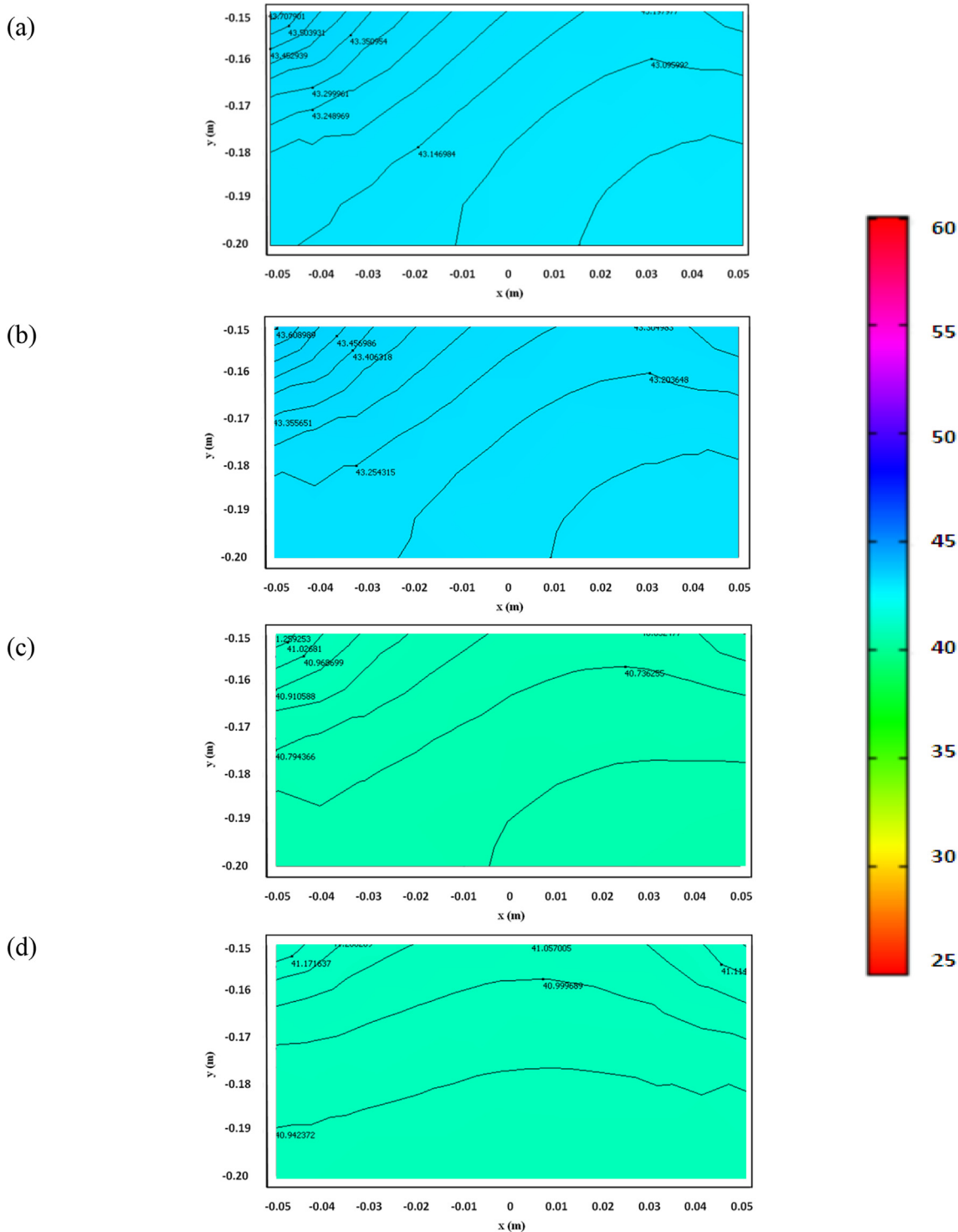


Fig. 19. Temperature distribution within water sample for 900 s in various θ ($V_0 = 20$ kV and $d = 4$ cm): (a) $\theta = 45^\circ$ (b) $\theta = 135^\circ$ (c) $\theta = 225^\circ$ and (d) $\theta = 315^\circ$.

heat to more transfer to the sample surface. This causes the temperature of sample to rapidly increase. In case of within the porous sample (Fig. 20), specific heat capacity of glass beads is lower than specific heat capacity of water so heating zone within the porous sample (Fig. 20) is higher than that in case of water sample (Fig. 19). In this study, sample properties are the main mechanism of the conduction term. Fig. 21

shows comparison of temperature ratio (average temperature within the water sample for EHD in various angles per average surface temperature of No EHD, $T_{s,avg}$) between water sample and porous sample and it is similar trends of comparison of average velocity field ratios within the sample. By the maximum velocity and maximum temperature are appeared in case of $\theta = 90^\circ$. So $\theta = 90^\circ$ is optimum electrode

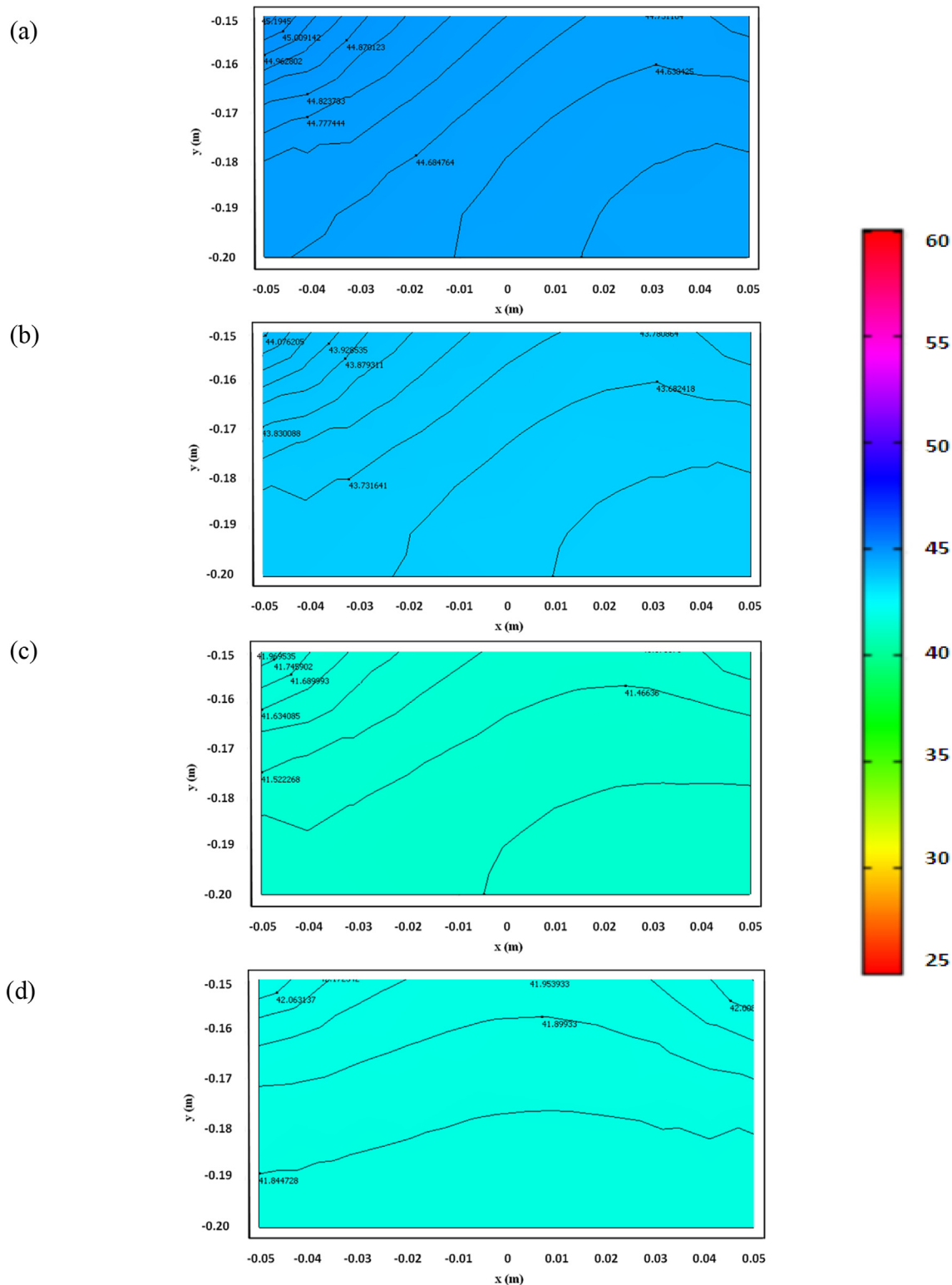


Fig. 20. Temperature distribution within porous sample for 900 s in various θ ($V_0 = 20$ kV and $d = 4$ cm): (a) $\theta = 45^\circ$ (b) $\theta = 135^\circ$ (c) $\theta = 225^\circ$ and (d) $\theta = 315^\circ$.

position due to it can induce the suitable electric force. The results show that the influence of swirling flow is affected with temperature distribution and heat transfer enhancement. In this study, fluid flow from swirling flow effect is the main mechanism of natural convection term. It is observed that conduction term within the sample is more effect than natural convection term.

7. Conclusion

Numerical simulation is carried out to study the influences of electrode arrangements and transport phenomena within the water and porous samples connected to rectangular duct under Electrohydrodynamics. The following are the conclusions of this work.

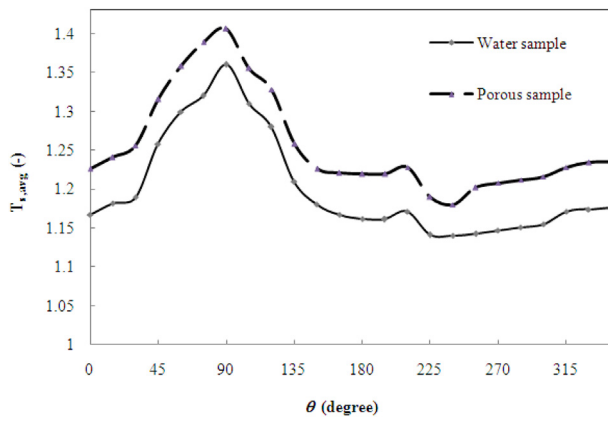


Fig. 21. Comparison of temperature ratio between within water sample and within porous sample when various θ .

1. The electric field from various angles can induce the difference swirling flow pattern within the rectangular duct. This is because electric force induces shear flow in different directions. By fluid flow within the sample are depended on the swirling flow and hot-airflow direction. The optimum electrode position is $\theta = 90^\circ$ due to it can induce the suitable electric force.
2. Electric force affects the swirling flow characteristics in relation to the heat transfer enhancement.
3. The velocity of fluid flow within the water sample is higher than within the porous sample because the natural convection is the main mechanism. But heating zone within the porous sample is higher than within the water sample because the conduction term is the main mechanism.

From above data, the idea behind this work can be used as guidance for special design for drying process. Electrohydrodynamics system is designed for drying industrial with the least manpower and minimum maintenance in the future.

Acknowledgement

The authors gratefully acknowledge the Thailand Research Fund (under the TRF contract No. TRG5780066 and RTA5980009) for their support of this study.

Appendix E. Supplementary data

Supplementary data related to this article can be found at <http://dx.doi.org/10.1016/j.ijthermalsci.2018.02.017>.

Nomenclatures

A	Area (m^2)
b	ion mobility ($m^2/V.s$)
C	Electricity capacity (C/V)
C_p	specific heat capacity (J/K)
D	electric flux density (C/m^2)
d	displacement between electrode and ground (cm)
E	electric field intensity (V/m)
EHD	Electrohydrodynamics
f_E	electric force ($C/m^2.s$)
h	height of wire (m)
h_c	convective heat transfer
J	current density (A/m^2)
k	thermal conductivity (W/m.K)
n	unit normal vector and coordinate in x and y axis
P	pressure (N/m^2)

Q	charge density (C)
q	space charge density (C/m^3)
T	uniform temperature (K)
T_∞	ambient temperature (K)
t	time (hr)
u	airflow velocity (m/s)
V	electrical voltage (V)
\forall	volume (m^3)
x, y	axis

Greek letters

ϵ	dielectric permittivity (F/m)
η	kinematics viscosity (m^2/s)
θ	angle between electrode and ground ($^\circ$)
μ	viscosity ($kg/m.s$)
ρ	density (kg/m^3)
φ	porosity (-)
κ	permeability (m^2)

Subscripts

d	lower interface
eff	effective value
i	inlet
l	liquid phase
s	solid, sample
u	upper interface
w	water sample
0	atmospheric, initial and wire

Superscript

T	transpose of matrix
---	---------------------

References

- [1] S.S. Siddhartha, R. Narasimha, A.J. Basu, S.V. Kailas, Coherent structures in numerically simulated jets with and without off-source heating, *Fluid Dynam Res* 26 (2000) 105–117.
- [2] M. Maskan, Drying, Shrinkage and rehydration characteristics of kiwifruits during hot air and microwave drying, *J Food Eng* 48 (2) (2001) 177–182.
- [3] M. Huang, F.C. Lai, Numerical study of EHD-enhanced water Evaporation, *J Electrostat* 68 (2010) 364–370.
- [4] H.A. Attia, Unsteady MHD flow near a rotating porous disk with uniform suction or injection, *Fluid Dynam Res* 23 (5) (1998) 111–125.
- [5] S. Markidis, G. Lapenta, R. Uddin, Multi-scale simulations of plasma with iPIC3D, *Math Comput Simulat* 80 (7) (2010) 1509–1519.
- [6] A. Yildirim, H. Askari, Z. Saadatnia, Y.M. Kalami, Y. Khan, Analysis of nonlinear oscillations of a punctual charge in the electric field of a charged ring via a Hamiltonian approach and the energy balance method, *Comp Math Appl* 62 (2011) 486–490.
- [7] A.P. Singh Bhalla, R. Bale, B.E. Griffith, N.A. Patankar, Fully resolved immersed Electrohydrodynamics for particle motion, Electrolocation, and self-propulsion, *J Comput Phys* 256 (1) (2014) 88–108.
- [8] P. Intra, A. Yawootti, P. Rattanadecho, Influence of the corona-wire diameter and length on corona discharge characteristics of a cylindrical tri-axial charger, *J Electrostat* 74 (2015) 37–46.
- [9] P. Rattanadecho, N. Suwannapum, W. Cha-um, Interaction between Electromagnetic and thermal fields in microwave heating of hardened type I-Cement paste using a rectangular waveguide, *ASME Trans. J Heat Transfer* 131 (2009) 082101-1-082101-12.
- [10] K. Chaiyo, P. Rattanadecho, Numerical analysis of heat-mass transport and pressure buildup of unsaturated porous medium in a rectangular waveguide subjected to a combined microwave and vacuum system, *Int J Heat Mass Tran* 34 (2013) 826–844.
- [11] N. Sakai, T. Hanzawa, Application and advances in infrared heating in Japan, *Trends Food Sci Technol* 5 (11) (1994) 357–362.
- [12] A. Yabe, Y. Mori, K. Hijikata, EHD study of the corona wind between wire and plate electrodes, *AIAA J* 16 (1978) 340–345.
- [13] G.S. Dulikravich, V. Ahuja, S. Lee, Modeling of dielectric fluid solidification with charged particles in electric fields and reduced gravity, *Numer Heat Tran B* 25 (1994) 353–373.
- [14] M.R. Vilela, J. Dente, Boundary-layer control by electric fields: a feasibility study, *ASME Trans. J. Fluids Eng.* 120 (1998) 626–629.

- [15] J.S. Chang, D. Brocilo, K. Urashima, J. Dekowski, J. Podlinski, On-set of EHD turbulence for cylinder in cross flow under corona discharges, *J Electrostat* 64 (2006) 569–573.
- [16] N. Takeuchi, K. Yasuoka, S. Ishii, Inducing mechanism of Electrohydrodynamic flow by surface barrier discharge, *IEEE Trans Plasma Sci* 35 (6) (2007) 1704–1709.
- [17] D.B. Go, R.A. Maturana, T.S. Fisher, S.V. Garimella, Enhancement of External forced convection by ionic wind, *Int J Heat Mass Tran* 51 (2008) 6047–6053.
- [18] N. Kasayapand, A computational fluid dynamics modeling of natural convection in finned enclosure under electric field, *Appl Therm Eng* 29 (2009) 131–141.
- [19] T. Wang, H. Li, Y. Zhang, D. Shi, Convective mode and electrical field in silicon melts under vertical, numer, *Heat Transfer* 67 (12) (2015) 1352–1369.
- [20] C. Chakranond, P. Rattanadecho, Analysis of heat and mass transfer enhancement in porous material subjected to electric fields (effects of particle sizes and layered arrangement), *Exp Therm Fluid Sci* 34 (2010) 1049–1056.
- [21] S. Saneewong Na Ayuttaya, C. Chakranond, P. Rattanadecho, T. Kreewatcharin, Effect of ground arrangements on swirling flow in a Channel subjected to Electrohydrodynamic effects, *ASME Journal of Fluids Engineering* 134 (2012) 051211–051219.
- [22] P. Intra, A. Yawootti, P. Rattanadecho, Numerical and experimental studies of collection efficiency of an ion electrostatic collector for a mini-volume electrical pm detector, *J Electrostat* 72 (2014) 477–486.
- [23] K.W.T. Christopher, D. Zhong, Wall boundary conditions for high-order finite-difference schemes in computational aeroacoustics, *Theor Comput Fluid Dynam* 6 (5) (1994) 303–322.
- [24] W.S. Seo, K. Yoshida, S. Yokota, K. Edamura, A high performance planar pump using Electro-conjugate fluid with improved electrode patterns, *Sensor Actuator* 134 (2007) 606–614.
- [25] H.H. Howard, D.J. Daniel, J.C. Marcel, Direct simulation of fluid particle motions, *Theor Comput Fluid Dynam* 3 (1992) 285–306.
- [26] L.C. Wen, J.J. Yuh, 3D numerical heat transfer and fluid flow analysis in plate-fin and tube heat Exchangers with Electrohydrodynamic enhancement, *Heat Mass Tran* 41 (2005) 583–593.
- [27] I.S. Shivakumara, M.S. Nagashree, K. Hemalatha, Electrothermoconvective instability in a heat generating dielectric fluid layer, *Int Commun Heat Mass Tran* 34 (9) (2010) 1041–1047.
- [28] S. Sungsoontorn, P. Rattanadecho, W. Pakdee, One-dimensional model of heat and mass transports and pressure Built up in unsaturated porous materials subjected to microwave energy, *Dry Technol* 29 (2011) 189–204.
- [29] D.J. Griffiths, *Introduction to Electrohydrodynamics*, Prentice Hall International, Inc, New Jersey, 1999.
- [30] P. Keangin, P. Rattanadecho, Analysis of heat transport on local thermal non-equilibrium in porous liver during microwave ablation, *Int J Heat Mass Tran* 67 (2013) 46–60.
- [31] L. Luc, M. Eric, A. Guillermo, T. Gerard, Influence of a DC corona discharge on the airflow along an inclined flat plate, *J Electrostat* 51–52 (2001) 300–306.